Geophysical Research Letters

RESEARCH LETTER
10.1029/2018GL081130

Slab Control on the Northeastern Edge of the Mid-Pacific LLSVP Near Hawaii

D. Sun[1,2], D. Helmberger[3], V. H. Lai[3], M. Gurnis[3], J. M. Jackson[3], and H.-Y. Yang[1,2]

[1]Laboratory of Seismology and Physics of Earth's Interior, School of Earth and Space Sciences, University of Science and Technology of China, Hefei, Anhui, China, [2]National Geophysics Observatory at Mengcheng, Mengcheng, Anhui, China, [3]Seismological Laboratory, California Institute of Technology, Pasadena, CA, USA

Key Points:
- Strong multipathing of ScS is observed near the northeastern edge of the mid-Pacific LLSVP
- A ULVZ located outboard from the LLSVP is required to explain the multipathed ScS
- Slab debris plays an important role in forming the complexity near the boundary of LLSVP

Supporting Information:
- Supporting Information S1

Correspondence to:
D. Sun,
sdy2014@ustc.edu.cn

Citation:
Sun, D., Helmberger, D., Lai, V. H., Gurnis, M., Jackson, J. M., & Yang, H.-Y. (2019). Slab control on the northeastern edge of the mid-Pacific LLSVP near Hawaii. *Geophysical Research Letters*, *46*, 3142–3152. https://doi.org/10.1029/2018GL081130

Received 29 OCT 2018
Accepted 13 FEB 2019
Accepted article online 15 FEB 2019
Published online 19 MAR 2019

Abstract At the core-mantle boundary, most observed ultralow velocity zones (ULVZs) cluster along the edges of the large low shear velocity provinces (LLSVPs) and provide key information on the composition, dynamics, and evolution of the lower mantle. However, their detailed structure near slab-like structures beneath the mid-Pacific remains particularly challenging because of the lack of station coverage. While most studies of ULVZs concentrate on SKS-complexity, here we report on the multipathing of ScS, which expands the sampling for ULVZs. We find the strongest multipathing along a ULVZ patch located just south of Hawaii and the far northeastern edge of the LLSVP, in a zone ~200 km in width and extending 600 km southward. The anomalous ScS travel times and distorted S_{diff} waveforms further reveal patches interrupted by observed enhanced D″ indicative of slab-debris influence on the complexity of the northeastern boundary of the mid-Pacific LLSVP.

Plain Language Summary Mapping the detailed boundaries of the large low shear velocity provinces at the core-mantle boundary is one of the keys to understanding the dynamics of the lower mantle. However, imaging the lower mantle beneath mid-Pacific is difficult because of the limited seismic ray coverage and seismic phases used. In this study, we identify a new seismic signal, multipathing of ScS, which can be modeled with an ultralow velocity zone sitting at the far edge of the mid-Pacific large low shear velocity province. The locations of the ultralow velocity zone and the nearby slab demonstrate that the complexities of the northeastern boundary of the mid-Pacific LLSVP are strongly affected by the slab reaching to the core-mantle boundary.

1. Introduction

Seismologists have revealed that the mantle side of the core-mantle boundary (CMB) region is extraordinarily complex with a myriad of fine structure (e.g., ~10 km to a few 100 km), such as large low shear velocity provinces (LLSVPs), ultralow velocity zones (ULVZs), and D″ layer. Thermal and chemical heterogeneity, solid-solid phase transitions, variations in the electronic state of Fe, anisotropy, a possible oxide-enriched basal layer, and melting within the lower mantle are probably all required in order to explain observed structures (Finkelstein et al., 2018; Garnero et al., 2016; Lay et al., 1998, 2008; Lay & Garnero, 2011). Understanding the origin of the fine-scale structure of the lower mantle, in general, and the D″ layer, in particular, is key toward understanding mantle convection. There is a great deal of research involved in defining both the relatively high seismic velocity anomalies around the Pacific thought to originate from the descent of subducted slabs into the lower mantle and the LLVSPs. By modulating the characteristics of the post-perovskite phase boundary, both structures have been inferred to influence the heat transfer across the CMB (Helmberger et al., 2005; Hirose, 2007; Murakami et al., 2005).

The detailed boundaries of the LLSVPs are crucial in developing a more realistic thermochemical model (Helmberger & Ni, 2005). A variety of studies have suggested that the LLSVPs are both thermally and chemically distinct features, but seismic studies have given inconclusive answers on the net density of the LLSVP (Koelemeijer et al., 2017; Lau et al., 2017), which is consistent with geodynamic models suggesting a balance between chemical and thermal forces (Tan & Gurnis, 2007). The LLSVP beneath southern Africa has the ideal data coverage with a seismic array above the structure that was used to study its sharpness, which is crucial to distinguishing between dynamic models for the origin of LLSVP with different edge sharpnesses and tilts depending on physical properties (Ni et al., 2002; Sun et al., 2009). Thus, relatively steep ray paths (such as SKS) can be used to define local boundary sharpness and small features such as ULVZs using the

SPdKS arrival. A more detailed review of the sharp edges of the LLSVP can be found in Text S1 in the supporting information (Davaille, 1999; French & Romanowicz, 2015; Garnero & McNamara, 2008; Grand, 2002; Ishii & Tromp, 1999; Lau et al., 2017; Masters et al., 2000; Montelli et al., 2006, 2004; Ritsema et al., 1998; Sun et al., 2010; Tan & Gurnis, 2005, 2007; Trampert et al., 2004; Wang & Wen, 2007). In contrast, the LLVSP beneath the mid-Pacific is more difficult to define because of the few seismic stations available regionally. The northeastern boundary of the mid-Pacific LLSVP beneath southeastern Hawaii has been extensively probed (Figure 1a), and many complexities have been revealed. Defining the boundaries of the mid-Pacific LLSVP has been difficult using seismic tomographic methods (Text S2), especially considering uncertainty in event locations caused by slab structure (Lu & Grand, 2016; Zhan et al., 2014). A more detailed discussion of the tomographic models can be found in Text S2 (Chu et al., 2017; Gaherty et al., 1996, 1999; Lai et al., 2017; Ritsema et al., 2011; Simmons et al., 2012; Tan & Helmberger, 2007).

Most observed ULVZs appear to be clustered at the margin of the LLSVPs, suggesting the formation of these ULVZs are linked to the LLSVP (Li et al., 2017; McNamara et al., 2010), while some ULVZs have been observed elsewhere (see recent review by Yu and Garnero, 2018). ULVZs are widely distributed along the northeastern edge of the mid-Pacific LLSVP. Luo et al. (2001) modeled the late PKP_{ab} arrival and associated waveform complexity by introducing a ULVZ (along boundary 1, Figure 1b) with a width of 150–300 km, height of 50 to 100 km and a P-velocity reduction of 8% to 12%. Such features involving late PKP_{ab} arrival, reduced amplitudes, and waveform complexity have been observed for the eastern most mid-Pacific structure (Sun et al., 2007). This PKP-inferred boundary from Luo et al.'s (2001) study is near the southern edge of a circular ULVZ with radius of ~500 km and height of ~20 km, proposed to explain late arrivals observed in *S* wave-diffracted coda (Cottaar & Romanowicz, 2012). Other localized ULVZs (shapes labeled 3–5 in Figure 1b) have been reported using PcP/ScS precursor or postcursors (Avants et al., 2006; Courtier et al., 2007; Hutko et al., 2009; Kohler et al., 1997; Lay et al., 2006; Mori & Helmberger, 1995; Revenaugh & Meyer, 1997; Zhao et al., 2017) and ScS2/ScS travel times (Liu et al., 2011). However, mostly layered ULVZ structures of the northeastern edge of the mid-Pacific LLSVP have been assumed. Here we demonstrate that the multipathing of ScS (called ScS*) provides a new constraint on the detailed geometry of the ULVZ at this key transition. In particular, we have used this phase to refine the northeastern edge of the mid-Pacific LLSVP just south of Hawaii to investigate the dynamic interactions between ULVZs, LLSVP, and the surrounding subducted slabs.

2. Data and Travel Times of ScS/S

We use deep focus earthquakes from a cluster beneath the Fiji-Tonga region and recorded in North America by the USArray (Figure S1 and Table S1). Most of the events are at relatively long period, 6 s and longer (e.g., Figure S4, event D). We use an algorithm known as the multipath detector (MPD) (Sun et al., 2009; Sun & Helmberger, 2011) to determine the ScS-S differential travel time residuals ($\delta t_{ScS\text{-}S}$) referenced to the CMB bounce points of ScS (Figure 2a). The $\delta t_{ScS\text{-}S}$ values are primarily controlled by ScS and the passage of the wave through the lowermost mantle (Figure S5). The largest delays are localized near the edge (circled by thin magenta dashed lines, Figure 2a). The southeastern patch with strong $\delta t_{ScS\text{-}S}$ delays overlapped with earlier sparser sampling (Figure 1b) showing similar strong delays (Russell et al., 1998). Such strong variation in $\delta t_{ScS\text{-}S}$ is difficult to explain by large-scale tomography inversions. These data appear to be strongly influenced by the detailed geometry of the transition boundary (TB) at the northeastern edge of the LLSVP (Figure 2a). Although differential travel times are predicted by smooth tomography models (GyPSuM; Simmons et al., 2010; Figures S6 and S7) and a modified S20RTS model (Ritsema et al., 2004) along this corridor (Liu et al., 2011), they do not account for the great complexity of ScS waveforms near the TB (Figure S6). Note that event A is located such that ScS is mainly sampling inside the LLSVP relative to B and C (Figure 1c) and its $\delta t_{ScS\text{-}S}$ values are small, indicating that the smooth tomography (GyPSuM) is doing well away from the TB as pointed out in He and Wen (2012). The travel time anomalies vary not only in distance but in azimuth as well, indicating the 3-D nature of the structure (Figures S7 and S8). In addition, an abrupt change in timing ($\delta t_{ScS\text{-}S}$) occurs near the azimuth of 38° (Figure 2a). The rapid azimuthal change is particularly obvious in stacks of the dense arrays, as displayed for the event B (Figure 2b); see Figure S9 for events A and C. Such strong variation at the CMB can produce strong multipathing as addressed in the next section.

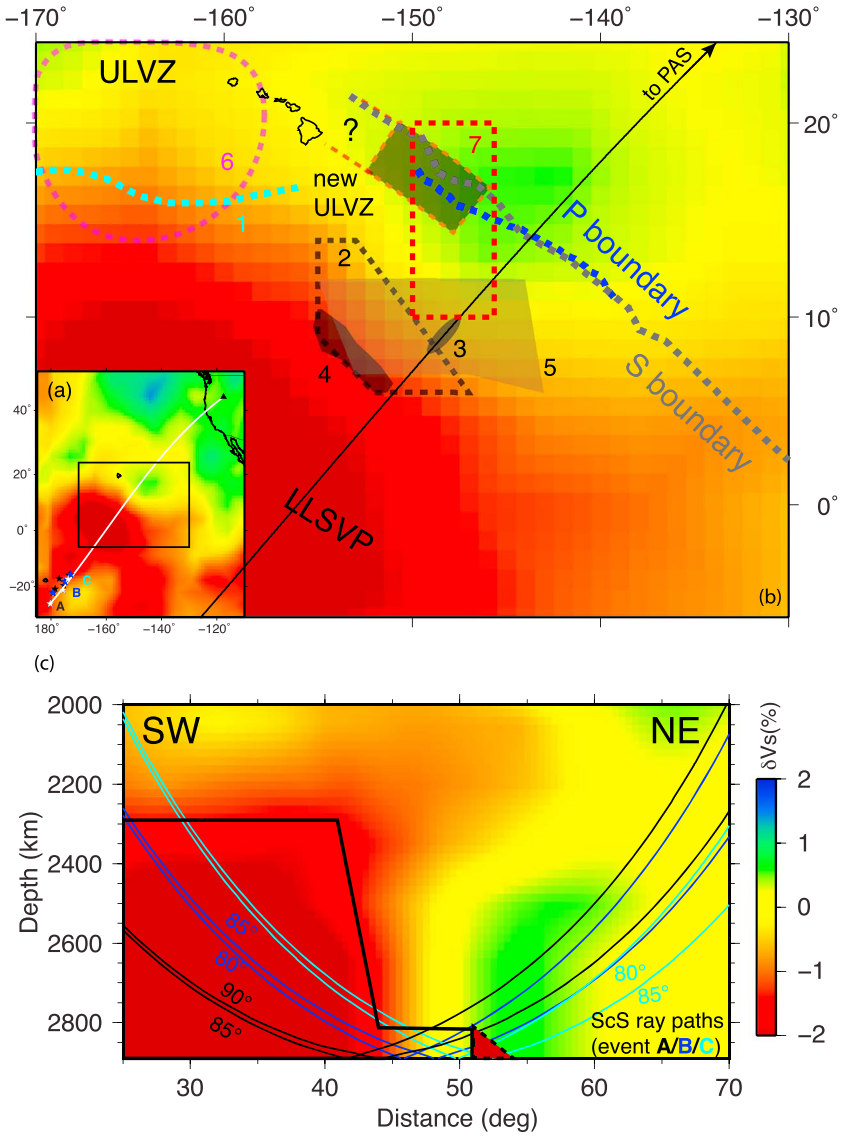

Figure 1. Distribution of events and stations used in this study along with the mapped ultralow velocity zones (ULVZs) along the northeastern edge of the mid-Pacific large low shear velocity province (LLSVP). (a) The locations of the events (stars) and the representative great circle paths (white line) to the USArray station (black triangle). Three events (A, B, and C) along the indicated great circle are modeled in detail. (b) Enlargement of the area marked with the black box in (a). The background tomographic image is from the GyPSuM model at the core-mantle boundary. The *S* wave (He & Wen, 2012) and *P* wave (Frost & Rost, 2014) boundary of the Pacific LLSVP are indicated by thick gray and blue dashed line. The cyan dashed line 1 displays the boundary inferred by Luo et al. (2001). The dashed polygon 2 area of strongly varied D″ structure (Lay et al., 2006). The shaded gray region inferred ULVZs: 3 (Liu et al., 2011), 4 (Avants et al., 2006; Courtier et al., 2007; Hutko et al., 2009; Kohler et al., 1997; Lay et al., 2006; Mori & Helmberger, 1995; Revenaugh & Meyer, 1997), and 5 (Zhao et al., 2017). The large ULVZ of Cottaar and Romanowicz (2012) as magenta circle 6. Newly mapped ULVZ marked as shaded gray rectangle bounded by orange dash lines. Red box 7 marks base of modeled Hawaii plume (Hassan et al., 2016). (c) Cross sections through hybrid model (GyPSuM tomography) plus uniform −2.5% shear velocity perturbation within black lines. At the tip of the LLSVP, a ULVZ (dashed black triangle) with δVs = −15% is required to explain the observed ScS*. Example ScS raypaths are shown as solid lines.

3. Modeling the Multipathing of ScS

We observed a distinct second arrival arriving after the reflection ScS, which we call ScS*, near the TB (Figure 2b). The behavior of ScS* changes rapidly for different event locations, indicating the importance of the geometry along the path from the source to the TB (Figure 3). The delayed ScS-S travel times and

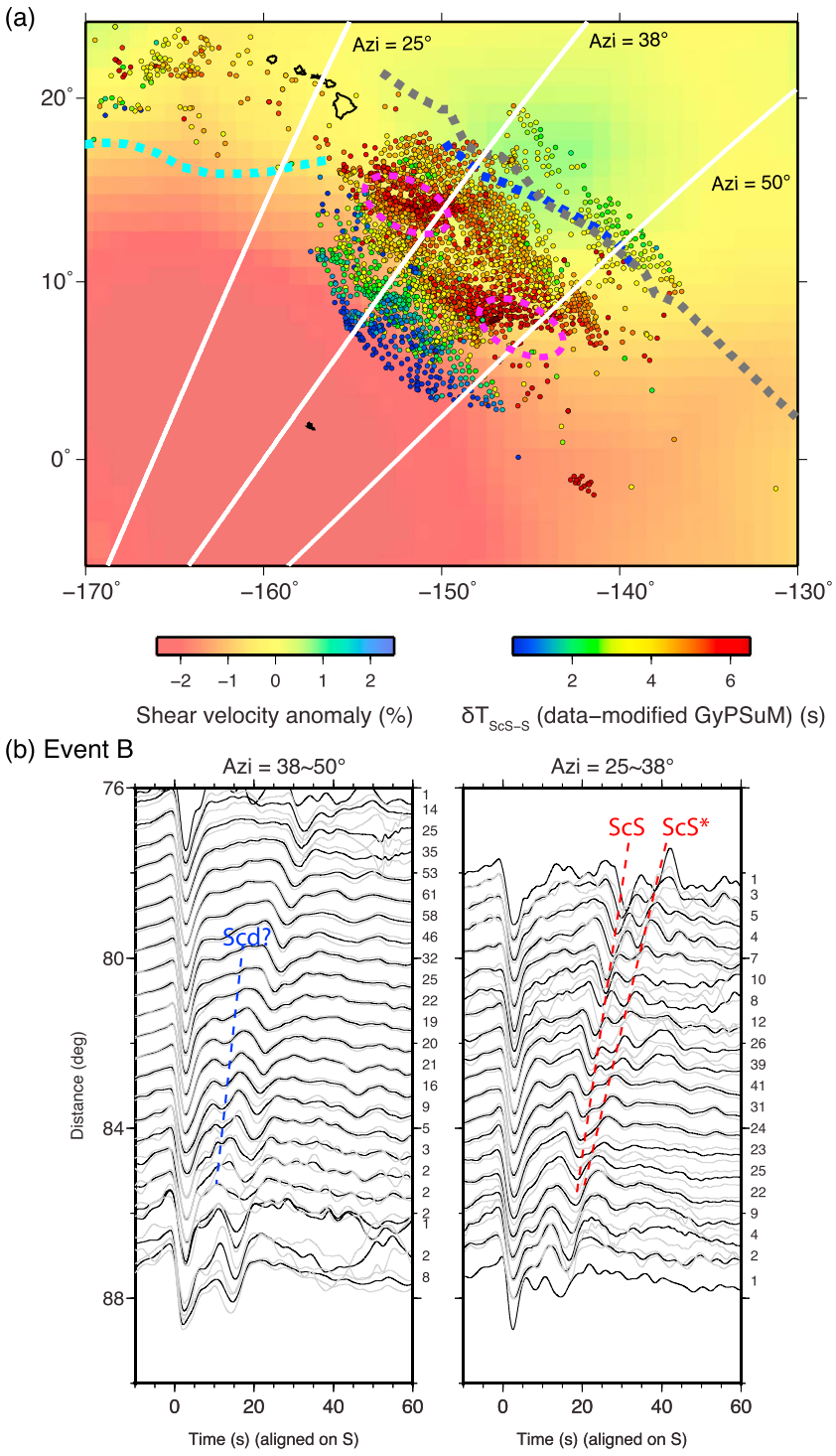

Figure 2. Measurements of ScS-S differential travel time residual ($\delta_{ScS\text{-}S}$). (a) $\delta_{ScS\text{-}S}$ values mapped to ScS core-mantle boundary reflected points. $\delta_{ScS\text{-}S}$ values are corrected for the effects of heterogeneities assuming GyPSuM from surface to the depth of 1,891 km and Preliminary Reference Earth Model (PREM) for the rest of the mantle to correct the effect of seismic heterogeneities at the shallow mantle. Two regions with dashed magenta ellipse have $\delta_{ScS\text{-}S}$ delayed up to 6 s, suggesting possible ultralow velocity zones. Boundary of large low shear velocity province displayed as gray dashed line from *S* wave study (He & Wen, 2012), blue dashed line from *P* wave study (Frost & Rost, 2014), and cyan dashed line from PKP study (Luo et al., 2001). Panel (b) displays the data stacks (black traces) for two azimuth ranges in (a) with gray traces indicating the 95% confidence limits. Number after each trace indicates the number of stacked records. Note the large azimuth of 38–50° has simple ScS arrivals, but the small azimuth of 25–38° has an extra arrival (ScS*) after the ScS arrivals (marked with red dashed lines).

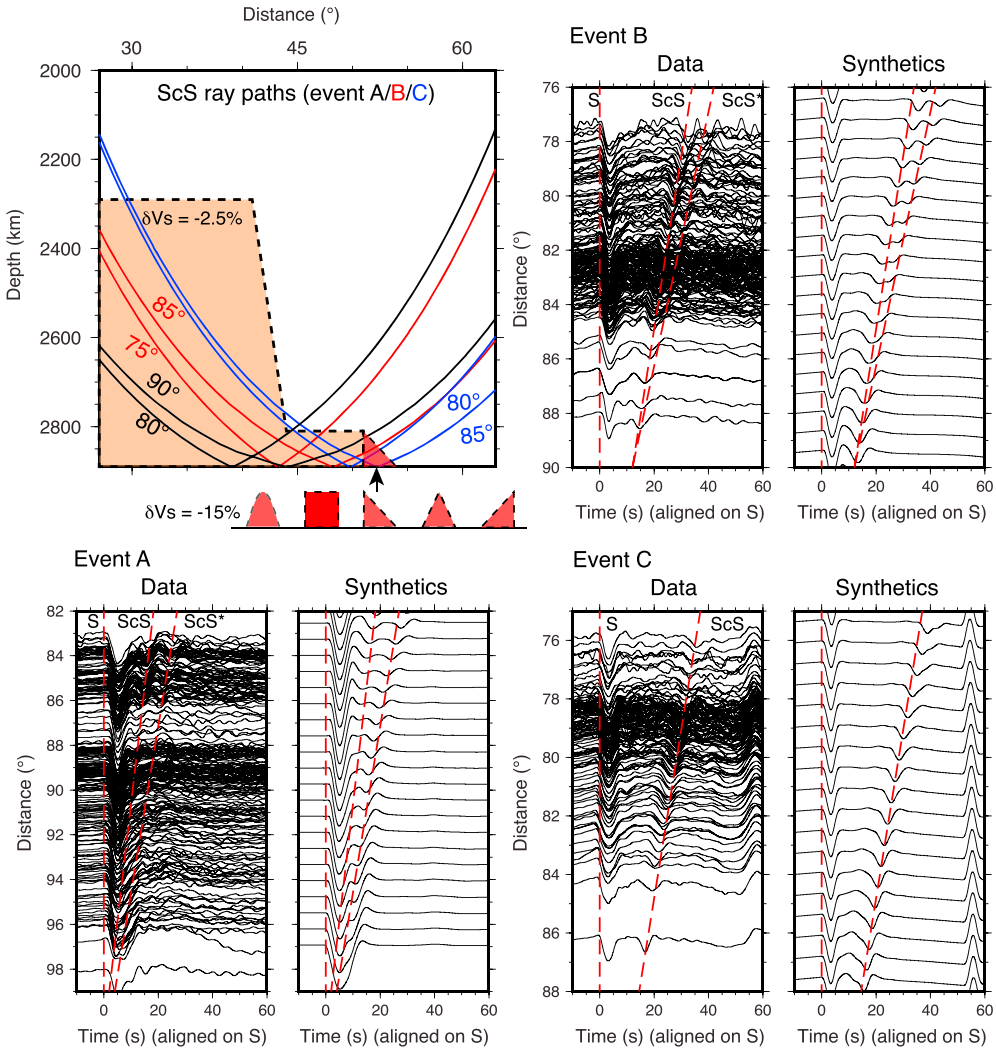

Figure 3. Waveform modeling of ScS for three events. Black traces are data, and red traces are synthetics. The ultralow velocity zone (ULVZ) at the edge of the large low shear velocity province (LLSVP) acting as a scatterer produces strong ScS* for events A and B. Note the waveforms of ScS* are not sensitive to the shapes of the ULVZ, such as dome, triangle, and rectangle, (Figure S13). At larger distance, ScS* moves close to the ScS with the rays getting close to the ULVZ (Figure 1c). For event C, ScS* is only presented at the smaller distances. Note the shape of the LLSVP here is purely derived from fitting the travel time of ScS-S, which may not properly represent the real structure, such as the thin elongated low velocity zone connecting the main structure of the LLSVP and the ULVZ.

small amplitude of ScS also suggest complex CMB structure. Three events (Figure 1a; events A, B, and C in Table S1) with the shortest source durations were chosen for detailed waveform modeling.

These events display the strongest variation in waveforms and sample the TB edge structure. To simulate these waveforms, we use a 2-D finite difference code with correction for 3-D spreading that runs on GPU machines (Li, Helmberger, et al., 2014). The code can generate core phases from 50 s to 3 Hz (Li, Sun, et al., 2014) and is highly efficient. It was used extensively in recent studies of lower mantle structures beneath Alaska (Sun et al., 2016) and southeastern United States (Ko et al., 2017). The modeling approach followed here is similar in that we rely on the latest tomographic images to inspire modifications by numerous forward-modeling tests. In modeling the ScS*, we only changed the V_S in the ULVZ.

We concentrate on modeling the multipathing in the corridor covered by the azimuth of 25–38° (Figure 2b). Stacked data are primarily used to forward model the details of the ULVZ (Figure S9). However, the stacking processes can weaken ScS* when aligning on S arrivals. Thus, the original data and synthetics are presented

in Figure 3 to highlight the variation of ScS*. Although this portion of the TB is particularly complicated, multipathed ScS is consistent with a forward hybrid model made by combining GyPSuM with a localized ULVZ structure (Figure 3). In the model, the ULVZ located at the far edge of the LLSVP produces a strong seismic scatterer at the CMB, reflecting energy as ScS*; thus, the ScS* varies rapidly depending on how ScS samples the ULVZ. Event A mostly samples beneath the LLSVP and only catches the ULVZ edge at the larger distance ranges 82° to 88°. Event B is the most sensitive and has the strongest ScS* arrivals. Event C samples nearly on top of the ULVZ; in this case, the ScS is just late and relatively simple. Other events display similar behavior with the strongest longer periods ScS combinations producing the late arrivals (Figure S10).

3.1. Location of the ULVZ

The detailed shape, boundary, and velocity structure of the LLSVP are not resolvable with the ray geometries at these periods (>5 s) as presented in Figure S11. We tested models with different velocity structures of the LLSVP. The synthetics generated from the hybrid model in Figure 3 fits the data about the same as the GyPSuM model plus the ULVZ (Figure S11). Even with an enhanced LLSVP at the bottom 660 km from the GyPSuM model or a simple IASP91 model, the waveform of the ScS and ScS* is almost identical to the original tomography model despite delayed ScS relative to S. Thus, our inference of ULVZ physical properties and location is based on the GyPSuM model plus the ULVZ for discussing sensitivity of model parameters. To quantify the goodness of the fit, we focus on event B, where the waveform distortions are the strongest, and calculate a cross-correlation coefficient (CC) between each stacked trace and synthetic seismograms at the same distance (Figure S12). Then the CCs of each trace is averaged over the record section for various models. If we cross-correlated the whole waveform including all phases, the CCs will be dominated by the large amplitude S and ScS. Thus, we focus on fitting the multipathing ScS by only cross-correlating the time window including ScS and ScS* considering the uncertainties in resolving the structure of the LLSVP.

3.2. Uniqueness of Shape

The geometrical shape of the ULVZ is difficult to resolve at these periods similar to the effects on the SKPdS/SPdKS waveform distortions (Wen & Helmberger, 1998). We explored the influence of ULVZ shape on synthetics, including a dome, symmetric triangle, right triangle, and rectangle (Figure S13); the responses are all comparable to the best fitting model with similar CCs. In contrast, a layered ULVZ will generate strong positive arrivals before as well as the prolonged arrivals after the ScS (Figure S14). Also, layered ULVZ models have a constant delay between ScS* and S, and wide rectangular ULVZ models have an extra arrival following the ScS*, which are not observed in the data (Figures S14–S16). Thus, we will assume that the ULVZ has a left triangular shape for further calculations and modify only its height (H), position (the distance from the event A to the left side of the ULVZ, Loc), width (w), and shear velocity perturbation (δV_S). ScS* arrivals earlier with smaller H and later with larger H (Figure S17a). Changing the δV_S produces similar effects. In Figure S17b, a set of models with different combination of H and δV_S can produce similar waveforms. However, a thin ULVZ with thickness of 20 km (second column in Figure S17b) with strong velocity perturbation produces secondary arrivals after the ScS* for both events B and C.

Our preferred structure with high CCs in waveforms is 150 km wide and 80 km high with a shear velocity reduction of 15% (Figures S17a–S17e). The synthetics with a stronger δV_S but closer ULVZ along with a weaker δV_S but larger Loc are compared to the preferred location at 51° for events A and B (Figure S17d). However, such models have difficulties in explaining the data of event C due to the faster ScS arrivals at larger distance. A model with a stronger δV_S and smaller Loc delays the ScS arrivals and also generates more complicated waveforms. However, strong trade-off between w and δV_S exists. In Figure S17e, all models with various combinations of w and δV_S produce almost identical waveforms for all three events. Thus, the sensitivity to location is the most important (Figures S18 and S19 and Text S3 for details). If the ULVZ is located inside of the LLSVP, small Loc, ScS* delays more relative to ScS at larger distances (Figures S15 and S17c), and the CC is significantly reduced (Figure S18) for either triangular or rectangular shapes. In this case, the synthetics are compared to the preferred location of a ULVZ of 51° from event A (Figure 3), positioned outboard from the LLSVP. Given such nonuniqueness, we can define a more useful parameter related to the delay of ScS* relative to the ScS, slowness volume (δV), defined by the product of width (w), height (H),

and the velocity reduction (δV_S) of the ULVZ. The best fits occur for δV near 3,000 (Figure S19). In short, a shear velocity reduction of 15% with a width of 3° and height of 80 km fits well.

4. Discussion

The ULVZ structure derived here appears to have properties related to those found beneath Iceland and other locations near the edges of LLVSPs. Although issues of shape resolution in modeling SPdKS data exist, the preferred ULVZ models tend to be stronger (30% to 15%) and thinner (40 km instead of 80 km) with comparable widths. Some of the ULVZs discussed above could be caused by the introduction of iron-rich oxide or incoming slab debris. That is, the ULVZ could be strongly affected by a superheated heavy mixture (Wicks et al., 2010). While density differential does not produce strong effects in ScS (SH) modeling, it plays a fundamental role in controlling shapes (Bower et al., 2011). Differences are expected based on thermal environments and accommodated by various aspect ratios of the shape (Bower et al., 2011). In particular, regions away from LLSVPs can produce piles as high as 80 km with a velocity reduction of 8% near slab debris, super heating, or both (Sun et al., 2013). If this is the case, we would expect strong variation in other seismic phases.

Indeed, evidence of lateral variation of the TB can be observed in the diffracted S data. For example, while these waveforms are complex along some azimuths, other samples are quite simple and can be predicted with the GyPSuM model (Figure S20). Figure 4a displays a comparison between diffracted SV and SH at the azimuth of 50–51°. Adding the D″ discontinuity in the original GyPSuM model by a phase boundary mapping only considering temperature effect (Sidorin et al., 1999) and a more complex mapping including possible chemical effect (Sun & Helmberger, 2008), referred to as TPT and CPT (Figure S21), predicts both the travel time differences and some of the added waveform complexity (Figure 4a), which is in agreement with the apparent splitting of *S* waves such as discussed in Parisi et al. (2018). Note the mapped D″ model can also generate the Scd arrivals (Figure S21) as observed for event B at the azimuth of 38–50° (Figure 2b). Although it is difficult to link the D″ discontinuity directly to the subduction at the CMB, a slab environment favors the appearance of the D″ as suggested by recent experimental study on the phase transition from (Fe,Al)-bridgmanite to postperovskite (Sun et al., 2018). While differences exist among different tomography models (Figure S3), there are substantial evidences for possible slab debris near the TB as indicated in the tomography (Figure 1) and in dynamic models (Hassan et al., 2016). Our inferred D″ region is also coincident with the D″ observation in Lay et al. (2006) (Figure 1), which is indicated as a subduction-driven flow at the edge of the LLSVP. The addition of slab material can greatly impact such phase boundary mapping (Sun et al., 2016), thus making the TB variable in 3-D. Some of the TB characteristics can be obtained by applying a MPD analysis on both SH and SV data (Figure 4b). Many of these travel time (Δ_T) comparisons indicate that SV arrives earlier than SH (Figure 4b) as evident in Figure 4a. Migration of these Δ_T shifts between SV and SH at their refracted midpoints at the CMB (Figure 4b) shows that the strongest anomalies are south of the multipathed ScS locations (black box in Figure 4b) and apparently associated with the prominent high seismic velocity zone given in some of the tomographic models of Figure 1c.

Essentially, the transition from the LLSVP to the neighboring structure is rapid, consistent with the $\delta t_{ScS\text{-}S}$ observations at other locations along the mid-Pacific LLSVP (He & Wen, 2012) and *P* wave travel times (Frost & Rost, 2014). Furthermore, Frost and Rost (2014) suggested that there is a correlation between the sharpness and the slope of the LLSVP walls where sharp TBs seem to have steep slopes, in general. However, such a relationship is difficult to define, given the errors in only working with travel times and uncertainties in event locations and origin times. Assuming Frost and Rost's (2014) statement on the slope of the LLSVP together with our new observations on the location of the D″ discontinuity and ULVZ, we hypothesize that when relatively cold and hence seismically high velocity, subducted blocks encounter the LLSVP (Figure 5), the walls of the LLSVP become steep (with slopes spread over ~40 km) where they are otherwise more gentle (~120 km). The negatively buoyant subducted material is expected to push the less viscous pile and ULVZ and sharpen the boundary (Davies & Gurnis, 1986; Tackley, 2002). Such a situation has been supported by time-dependent spherical models (Bower et al., 2013; McNamara & Zhong, 2005; Tan et al., 2011), unless the base of the putative chemical anomaly associated with the LLSVP is too dense. In contrast, without a slab-induced indentation, the more appropriate (and perhaps more common) scenario

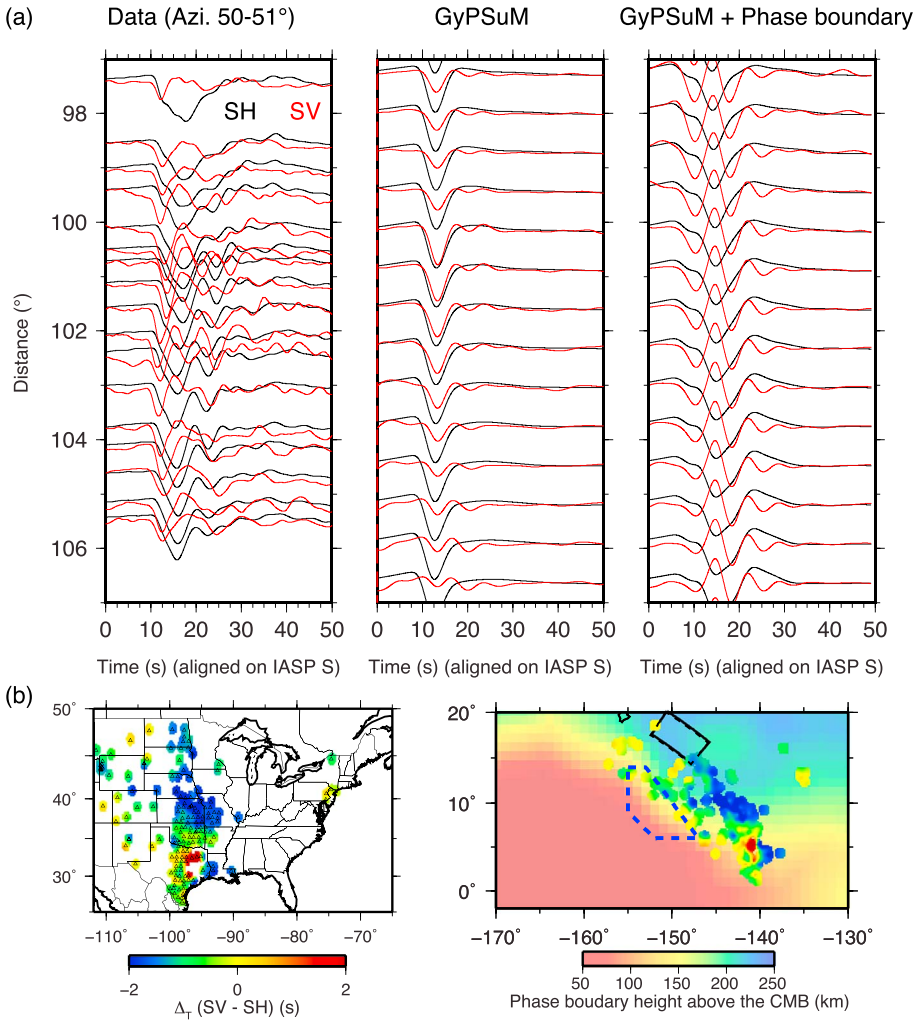

Figure 4. Observed complexities of the diffracted *S* at the edge of the large low shear velocity province. (a) Comparison between the diffracted SH and SV of the event L (Table S1). Black traces are SH and red traces are SV. The observed SV faster than SH in the data is not predicted by the GyPSuM model. By adding a phase boundary at the bottom of the GyPSuM model (Figure S21), we can explain the difference between SH and SV well (Parisi et al., 2018). (b) Measured travel time difference between SV and SH (Δ_T [SV-SH]) plotted at the stations (left) and the middle point of the S_{diff} at the core-mantle boundary (right). The background color in the right figure indicates the height above the core-mantle boundary of mapped D″ discontinuity. The polygon with blue dashed line displays the strongly varied D″ structure beneath the central Pacific (Lay et al., 2006). The new mapped ultralow velocity zone is marked as a rectangle bounded by black lines.

has the distal ULVZ located at the outer edge of the TB (Figure 5). This structure is supported by our observations of the ULVZ here. This structure could either be swept by the convection flow in the LLSVP (Li et al., 2017; McNamara et al., 2010) or entrained back into the background (Bower et al., 2011).

The localized ULVZ may be the root for the hot upwelling plume (Helmberger et al., 1998; Yu & Garnero, 2018; Yuan & Romanowicz, 2017). At the same time, slabs likely play an active role while interacting with LLSVPs and influence the locations of ULVZ. Such shifts at the northeastern edge of mid-Pacific LLSVP agree with the possible Hawaiian-Emperor hot spot track explanation, which appears to be directly related to the subduction history in the North Pacific since 100 Ma (Hassan et al., 2016). The position may be coincidental, but we note that the position of the present plume origin from geodynamic models, which fit the hot spot track of the Hawaiian-Emperor chain from Hassan et al. (2016) (pink box 7 in Figure 1b), is located near the high velocity indentation structure. Hassan et al. (2016) further suggested that the origin of the Hawaiian plume in D″ changes over time based on the interaction of subducted slabs. Subduction history

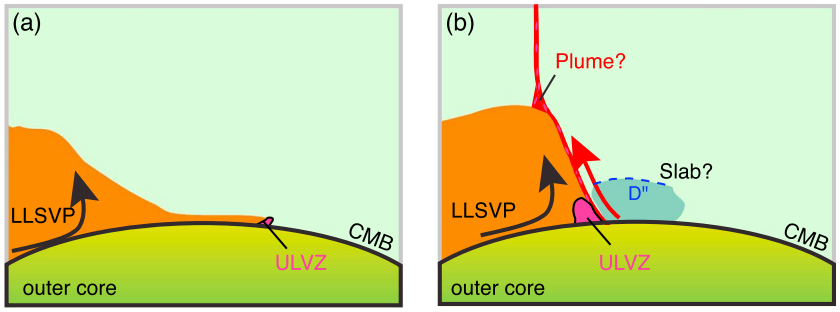

Figure 5. Interpreted images of the relative locations of ultralow velocity zone (ULVZ) and large low shear velocity province (LLSVP). In an average mantle, the ULVZ locates at the far edge of the LLSVP (left). While a strong D″ (possible slab debris) is present near the edge of the LLSVP, a steepened edge of the LLSVP may develop (Frost & Rost, 2014), and the ULVZ may be driven towards the interior of the LLSVP, and develop a possible plume. CMB = core-mantle boundary.

plays a major role in shaping the edges and possible migration of the plume source, and we suggest that further seismic modeling, including the mapping of ScS*, can help define such features.

5. Conclusions

In this paper, we present observations of multipathed ScS on SH data of USArray and flex arrays for the Fiji-Tonga earthquakes. Detailed modeling of the ScS* allows us to constrain the location of the ULVZ, just southeast of Hawaii and the far edge of the mid-Pacific LLSVP, roughly 150 km across. While there are the usual trade-offs among the parameters defining ULVZ, a ULVZ with a height of 80 km with an *S*-velocity reduction of 15% fits the data best. The locations of ULVZs and the identified D″ structures suggest that the complexities of the northeastern boundary of the mid-Pacific LLSVP are strongly affected by the slab reaching the CMB.

Acknowledgments
The authors would like to thank Editor Jeroen Ritsema and two anonymous reviewers. Their suggestions and comments were greatly appreciated and lead to significant improvements to the manuscript. We thank the IRIS Data Center and Earthscope USArray for providing the seismic data, which are available at the IRIS website (http://www.iris.edu). All maps in this paper were produced using GMT developed by Paul Wessel and Walter H.F. Smith. We are thankful to Strategic Priority Research Program (B) of Chinese Academy of Sciences, Grant XDB18000000; National Natural Science Foundation of China 41574037; Chinese MOST 973 program 2014CB845901; Key Research Program of Frontier Sciences CAS, Grant QYZDB-SSWSYS011; Fundamental Research Funds for the Central Universities in China WK2080000078; and the NSF CSEDI EAR-1161046 for support of this research.

References

Avants, M., Lay, T., & Garnero, E. J. (2006). A new probe of ULVZ S-wave velocity structure: Array stacking of ScS waveforms. *Geophysical Research Letters*, *33*, L07314. https://doi.org/10.1029/2005GL024989

Bower, D. J., Gurnis, M., & Seton, M. (2013). Lower mantle structure from paleogeographically constrained dynamic earth models. *Geochemistry, Geophysics, Geosystems*, *14*, 44–63. https://doi.org/10.1029/2012GC004267

Bower, D. J., Wicks, J. K., Gurnis, M., & Jackson, J. M. (2011). A geodynamic and mineral physics model of a solid-state ultralow-velocity zone. *Earth and Planetary Science Letters*, *303*, 193–202. https://doi.org/10.1016/j.epsl.2010.12.035

Chu, R., Ko, J. Y.-T., Wei, S., Zhan, Z., & Helmberger, D. (2017). Lithospheric radial anisotropy beneath the Gulf of Mexico. *Earth and Planetary Science Letters*, *466*, 43–52. https://doi.org/10.1016/j.epsl.2017.02.040

Cottaar, S., & Romanowicz, B. (2012). An unusually large ULVZ at the base of the mantle near Hawaii. *Earth and Planetary Science Letters*, *355-356*, 213–222. https://doi.org/10.1016/j.epsl.2012.09.005

Courtier, A. M., Bagley, B., & Revenaugh, J. (2007). Whole mantle discontinuity structure beneath Hawaii. *Geophysical Research Letters*, *34*, L17304. https://doi.org/10.1029/2007GL031006

Davaille, A. (1999). Simultaneous generation of hotspots and superswells by convection in a heterogenous planetary mantle. *Nature*, *402*(6763), 756–760. https://doi.org/10.1038/45461

Davies, G. F., & Gurnis, M. (1986). Interaction of mantle dregs with convection: Lateral heterogeneity at the core-mantle boundary. *Geophysical Research Letters*, *13*(13), 1517–1520. https://doi.org/10.1029/GL013i013p01517

Finkelstein, G. J., Jackson, J. M., Said, A., Alatas, A., Leu, B. M., Sturhahn, W., & Toellner, T. S. (2018). Strongly anisotropic Magnesiowustite in Earth's lower mantle. *Journal of Geophysical Research: Solid Earth*, *123*, 4740–4750. https://doi.org/10.1029/2017JB015349

French, S. W., & Romanowicz, B. (2015). Broad plumes rooted at the base of the Earth's mantle beneath major hotspots. *Nature*, *525*, 95–99. https://doi.org/10.1038/nature14876

Frost, D. A., & Rost, S. (2014). The P-wave boundary of the large-low shear velocity province beneath the Pacific. *Earth and Planetary Science Letters*, *403*, 380–392. https://doi.org/10.1016/j.epsl.2014.06.046

Gaherty, J. B., Jordan, T. H., & Gee, L. S. (1996). Seismic structure of the upper mantle in a central Pacific corridor. *Journal of Geophysical Research*, *101*(B10), 22,291–22,309. https://doi.org/10.1029/96JB01882

Gaherty, J. B., Kato, M., & Jordan, T. H. (1999). Seismological structure of the upper mantle: A regional comparison of seismic layering. *Physics of the Earth and Planetary Interiors*, *110*(1–2), 21–41. https://doi.org/10.1016/s0031-9201(98)00132-0

Garnero, E. J., & McNamara, A. K. (2008). Structure and dynamics of Earth's lower mantle. *Science*, *320*, 626–628. https://doi.org/10.1126/science.1148028

Garnero, E. J., McNamara, A. K., & Shim, S.-H. (2016). Continent-sized anomalous zones with low seismic velocity at the base of Earth's mantle. *Nature Geoscience*, *9*, 481–489. https://doi.org/10.1038/ngeo2733

Grand, S. P. (2002). Mantle shear-wave tomography and the fate of subducted slabs. *Philosophical Transactions of the Royal Society of London*, *360*(1800), 2475–2491. https://doi.org/10.1098/rsta.2002.1077

Hassan, R., Mueller, R. D., Gurnis, M., Williams, S. E., & Flament, N. (2016). A rapid burst in hotspot motion through the interaction of tectonics and deep mantle flow. *Nature*, *533*, 239–242. https://doi.org/10.1038/nature17422

He, Y., & Wen, L. (2012). Geographic boundary of the "Pacific Anomaly" and its geometry and transitional structure in the north. *Journal of Geophysical Research*, *117*, B09308. https://doi.org/10.1029/2012JB009436

Helmberger, D., Lay, T., Ni, S., & Gurnis, M. (2005). Deep mantle structure and the postperovskite phase transition. *Proceedings of the National Academy of Sciences of the United States of America*, *102*, 17,257–17,263. https://doi.org/10.1073/pnas.0502504102

Helmberger, D. V., & Ni, S. D. (2005). Seismic modeling constraints on the South African super plume. In R. D. VanDerHilst, J. D. Bass, J. Matas, & J. Trampert (Eds.), *Earth's deep mantle: Structure, composition, and evolution* (pp. 63–81). Washington, DC: Carnegie Institute of Washington.

Helmberger, D. V., Wen, L., & Ding, X. (1998). Seismic evidence that the source of the Iceland hotspot lies at the core-mantle boundary. *Nature*, *396*(6708), 251–255. https://doi.org/10.1038/24357

Hirose, K. (2007). Discovery of post-perovskite phase transition and the nature of D'' layer. In J. Brodholt, T. Lay, & D. A. Yuen (Eds.), *Post-Perovksite: The Last Mantle Phase Transition* (pp. 19–35). Washington, DC: American Geophysical Union. https://doi.org/10.1029/174GM04

Hutko, A. R., Lay, T., & Revenaugh, J. (2009). Localized double-array stacking analysis of PcP: D'' and ULVZ structure beneath the Cocos plate, Mexico, central Pacific, and north Pacific. *Physics of the Earth and Planetary Interiors*, *173*, 60–74. https://doi.org/10.1016/j.pepi.2008.11.003

Ishii, M., & Tromp, J. (1999). Normal-mode and free-air gravity constraints on lateral variations in velocity and density of Earth's mantle. *Science*, *285*(5431), 1231–1236. https://doi.org/10.1126/science.285.5431.1231

Ko, J. Y.-T., Helmberger, D. V., Wang, H., & Zhan, Z. (2017). Lower mantle substructure embedded in the Farallon Plate: The Hess conjugate. *Geophysical Research Letters*, *44*, 10,216–10,225. https://doi.org/10.1002/2017GL075032

Koelemeijer, P., Deuss, A., & Ritsema, J. (2017). Density structure of Earth's lowermost mantle from Stoneley mode splitting observations. *Nature Communications*, *8*, 15241. https://doi.org/10.1038/ncomms15241

Kohler, M. D., Vidale, J. E., & Davis, P. M. (1997). Complex scattering within D observed on the very dense Los Angeles region seismic experiment passive array. *Geophysical Research Letters*, *24*(15), 1855–1858. https://doi.org/10.1029/97GL01823

Lai, V. H., Graves, R. W., Wei, S., & Helmberger, D. (2017). Evidence for strong lateral seismic velocity variation in the lower crust and upper mantle beneath the California margin. *Earth and Planetary Science Letters*, *463*, 202–211. https://doi.org/10.1016/j.epsl.2017.02.002

Lau, H. C. P., Mitrovica, J. X., Davis, J. L., Tromp, J., Yang, H.-Y., & Al-Attar, D. (2017). Tidal tomography constrains Earth's deep-mantle buoyancy. *Nature*, *551*, 321–326. https://doi.org/10.1038/nature24452

Lay, T., & Garnero, E. J. (2011). Deep mantle seismic modeling and imaging. *Annual Review of Earth and Planetary Sciences*, *39*, 91–123. https://doi.org/10.1146/annurev-earth-040610-133354

Lay, T., Hernlund, J., & Buffett, B. A. (2008). Core-mantle boundary heat flow. *Nature Geoscience*, *1*, 25–32. https://doi.org/10.1038/ngeo.2007.44

Lay, T., Hernlund, J. W., Garnero, E. J., & Thorne, M. S. (2006). A post-perovskite lens and D'' heat flux beneath the central Pacific. *Science*, *314*, 1272–1276. https://doi.org/10.1126/science.1133280

Lay, T., Williams, Q., & Garnero, E. J. (1998). The core-mantle boundary layer and deep Earth dynamics. *Nature*, *392*(6675), 461–468. https://doi.org/10.1038/33083

Li, D., Helmberger, D., Clayton, R. W., & Sun, D. (2014). Global synthetic seismograms using a 2-D finite-difference method. *Geophysical Journal International*, *197*, 1166–1183. https://doi.org/10.1093/gji/ggu1050

Li, D., Sun, D., & Helmberger, D. (2014). Notes on the variability of reflected inner core phases. *Earthquake Science*, *27*, 441–468. https://doi.org/10.1007/s11589-014-0093-9

Li, M., McNamara, A. K., Garnero, E. J., & Yu, S. (2017). Compositionally-distinct ultra-low velocity zones on Earth's core-mantle boundary. *Nature Communications*, *8*, 177. https://doi.org/10.1038/s41467-017-00219-x

Liu, L., Tan, Y., Sun, D., Chen, M., & Helmberger, D. (2011). Trans-Pacific whole mantle structure. *Journal of Geophysical Research*, *116*, B04306. https://doi.org/10.1029/2010JB007907

Lu, C., & Grand, S. P. (2016). The effect of subducting slabs in global shear wave tomography. *Geophysical Journal International*, *205*, 1074–1085. https://doi.org/10.1093/gji/ggw072

Luo, S. N., Ni, S. D., & Helmberger, D. V. (2001). Evidence for a sharp lateral variation of velocity at the core-mantle boundary from multipathed PKPab. *Earth and Planetary Science Letters*, *189*(3–4), 155–164. https://doi.org/10.1016/s0012-821x(01)00364-8

Masters, G., Laske, G., Bolton, H., & Dziewonski, A. M. (2000). The relative behavior of shear velocity, bulk sound speed, and compressional velocity in the mantle: Implications for chemical and thermal structure. In S. Karato et al. (Eds.), *Earth's deep interior: Mineral physics and tomography from the atomic to the global scale, Geophysical Monograph Series* (pp. 63–87). Washington, DC: Amerian Geophysical Union. https://doi.org/10.1029/GM117p0063

McNamara, A. K., Garnero, E. J., & Rost, S. (2010). Tracking deep mantle reservoirs with ultra-low velocity zones. *Earth and Planetary Science Letters*, *299*, 1–9. https://doi.org/10.1016/j.epsl.2010.07.042

McNamara, A. K., & Zhong, S. J. (2005). Thermochemical structures beneath Africa and the Pacific Ocean. *Nature*, *437*(7062), 1136–1139. https://doi.org/10.1038/nature04066

Montelli, R., Nolet, G., Dahlen, F. A., & Masters, G. (2006). A catalogue of deep mantle plumes: New results from finite-frequency tomography. *Geochemistry, Geophysics, Geosystems*, *7*, Q11007. https://doi.org/10.1029/2006GC001248

Montelli, R., Nolet, G., Dahlen, F. A., Masters, G., Engdahl, E. R., & Hung, S. H. (2004). Finite-frequency tomography reveals a variety of plumes in the mantle. *Science*, *303*, 338–343. https://doi.org/10.1126/science.1092485

Mori, J., & Helmberger, D. V. (1995). Localized boundary-layer below the mid-pacific velocity anomaly identified from a PcP precursor. *Journal of Geophysical Research*, *100*(B10), 20,359–20,365. https://doi.org/10.1029/95JB02243

Murakami, M., Hirose, K., Sata, N., & Ohishi, Y. (2005). Post-perovskite phase transition and mineral chemistry in the pyrolitic lowermost mantle. *Geophysical Research Letters*, *32*, L03304. https://doi.org/10.1029/2004GL021956

Ni, S. D., Tan, E., Gurnis, M., & Helmberger, D. (2002). Sharp sides to the African superplume. *Science*, *296*(5574), 1850–1852. https://doi.org/10.1126/science.1070698

Parisi, L., Ferreira, A. M. G., & Ritsema, J. (2018). Apparent splitting of S waves propagating through an isotropic lowermost mantle. *Journal of Geophysical Research: Solid Earth*, *123*, 3909–3922. https://doi.org/10.1002/2017JB014394

Revenaugh, J., & Meyer, R. (1997). Seismic evidence of partial melt within a possibly ubiquitous low-velocity layer at the base of the mantle. *Science*, *277*(5326), 670–673. https://doi.org/10.1126/science.277.5326.670

Ritsema, J., Deuss, A., van Heijst, H. J., & Woodhouse, J. H. (2011). S40RTS: A degree-40 shear-velocity model for the mantle from new Rayleigh wave dispersion, teleseismic traveltime and normal-mode splitting function measurements. *Geophysical Journal International*, *184*, 1223–1236. https://doi.org/10.1111/j.1365-246X.2010.04884.x

Ritsema, J., Ni, S., Helmberger, D. V., & Crotwell, H. P. (1998). Evidence for strong shear velocity reductions and velocity gradients in the lower mantle beneath Africa. *Geophysical Research Letters*, *25*(23), 4245–4248. https://doi.org/10.1029/1998GL900127

Ritsema, J., van Heijst, H. J., & Woodhouse, J. H. (2004). Global transition zone tomography. *Journal of Geophysical Research*, *109*, L16311. https://doi.org/10.1029/2003JB002610

Russell, S. A., Lay, T., & Garnero, E. J. (1998). Seismic evidence for small-scale dynamics in the lowermost mantle at the root of the Hawaiian hotspot. *Nature*, *396*(6708), 255–258. https://doi.org/10.1038/24364

Sidorin, I., Gurnis, M., & Helmberger, D. V. (1999). Evidence for a ubiquitous seismic discontinuity at the base of the mantle. *Science*, *286*(5443), 1326–1331. https://doi.org/10.1126/science.286.5443.1326

Simmons, N. A., Forte, A. M., Boschi, L., & Grand, S. P. (2010). GyPSuM: A joint tomographic model of mantle density and seismic wave speeds. *Journal of Geophysical Research*, *115*, B12310. https://doi.org/10.1029/2010JB007631

Simmons, N. A., Myers, S. C., Johannesson, G., & Matzel, E. (2012). LLNL-G3Dv3: Global P wave tomography model for improved regional and teleseismic travel time prediction. *Journal of Geophysical Research*, *117*, B10302. https://doi.org/10.11029/12012JB009525

Sun, D., & Helmberger, D. (2008). Lower mantle tomography and phase change mapping. *Journal of Geophysical Research*, *113*, B10305. https://doi.org/10.1029/2007JB005289

Sun, D., & Helmberger, D. (2011). Upper-mantle structures beneath USArray derived from waveform complexity. *Geophysical Journal International*, *184*, 416–438. https://doi.org/10.1111/j.1365-246X.2010.04847.x

Sun, D., Helmberger, D., & Gurnis, M. (2010). A narrow, mid-mantle plume below southern Africa. *Geophysical Research Letters*, *37*, L09302. https://doi.org/10.1029/2009GL042339

Sun, D., Helmberger, D., Jackson, J. M., Clayton, R. W., & Bower, D. J. (2013). Rolling hills on the core-mantle boundary. *Earth and Planetary Science Letters*, *361*, 333–342. https://doi.org/10.1016/j.epsl.2012.10.027

Sun, D., Helmberger, D., Miller, M. S., & Jackson, J. M. (2016). Major disruption of D′′ beneath Alaska. *Journal of Geophysical Research: Solid Earth*, *121*, 3534–3556. https://doi.org/10.1002/2015JB012534

Sun, D., Helmberger, D., Ni, S., & Bower, D. (2009). Direct measures of lateral velocity variation in the deep earth. *Journal of Geophysical Research*, *114*, B05303. https://doi.org/10.01029/02008JB005873

Sun, N., Wei, W., Han, S., Song, J., Li, X., Duan, Y., Prakapenka, V. B., & Mao, Z. (2018). Phase transition and thermal equation of state of (Fe,Al)-bridgmanite and post-perovskite: Implication for the chemical heterogeneity at the lowermost mantle. *Earth and Planetary Science Letters*, *490*, 161–169. https://doi.org/10.1016/j.epsl.2018.03.004

Sun, X., Song, X., Zheng, S., & Helmberger, D. V. (2007). Evidence for a chemical-thermal structure at base of mantle from sharp lateral P-wave variations beneath Central America. *Proceedings of the National Academy of Sciences of the United States of America*, *104*, 26–30. https://doi.org/10.1073/pnas.0609143103

Tackley, P. J. (2002). Strong heterogeneity caused by deep mantle layering. *Geochemistry, Geophysics, Geosystems*, *3*(4), L07605. https://doi.org/10.1029/2001GC000167

Tan, E., & Gurnis, M. (2005). Metastable superplumes and mantle compressibility. *Geophysical Research Letters*, *32*, L20307. https://doi.org/10.1029/2005GL024190

Tan, E., & Gurnis, M. (2007). Compressible thermochemical convection and application to lower mantle structures. *Journal of Geophysical Research*, *112*, B06304. https://doi.org/10.1029/2006JB004505

Tan, E., Leng, W., Zhong, S., & Gurnis, M. (2011). On the location of plumes and lateral movement of thermochemical structures with high bulk modulus in the 3-D compressible mantle. *Geochemistry, Geophysics, Geosystems*, *12*, Q07005. https://doi.org/10.1029/2011GC003665

Tan, Y., & Helmberger, D. V. (2007). Trans-Pacific upper mantle shear velocity structure. *Journal of Geophysical Research*, *112*, B08301. https://doi.org/10.1029/2006JB004853

Trampert, J., Deschamps, F., Resovsky, J., & Yuen, D. (2004). Probabilistic tomography maps chemical heterogeneities throughout the lower mantle. *Science*, *306*, 853–856. https://doi.org/10.1126/science.1101996

Wang, Y., & Wen, L. (2007). Geometry and P and S velocity structure of the "African Anomaly". *Journal of Geophysical Research*, *112*, B05313. https://doi.org/10.1029/2007JB005220

Wen, L. X., & Helmberger, D. V. (1998). A two-dimensional P-SV hybrid method and its application to modeling localized structures near the core-mantle boundary. *Journal of Geophysical Research*, *103*(B8), 17,901–17,918. https://doi.org/10.1029/98JB01276

Wicks, J. K., Jackson, J. M., & Sturhahn, W. (2010). Very low sound velocities in iron-rich (Mg,Fe)O: Implications for the core-mantle boundary region. *Geophysical Research Letters*, *37*, L15304. https://doi.org/10.1029/2010GL043689

Yu, S., & Garnero, E. J. (2018). Ultralow velocity zone locations: A global assessment. *Geochemistry, Geophysics, Geosystems*, *19*, 396–414. https://doi.org/10.1002/2017GC007281

Yuan, K., & Romanowicz, B. (2017). Seismic evidence for partial melting at the root of major hot spot plumes. *Science*, *357*, 393–397. https://doi.org/10.1126/science.aan0760

Zhan, Z., Helmberger, D. V., & Li, D. (2014). Imaging subducted slab structure beneath the Sea of Okhotsk with teleseismic waveforms. *Physics of the Earth and Planetary Interiors*, *232*, 30–35. https://doi.org/10.1016/j.pepi.2014.03.008

Zhao, C., Garnero, E. J., Li, M., McNamara, A., & Yu, S. (2017). Intermittent and lateral varying ULVZ structure at the northeastern margin of the Pacific LLSVP. *Journal of Geophysical Research: Solid Earth*, *122*, 1198–1220. https://doi.org/10.1002/2016JB013449